Heterogeneous & Homogeneous & Bio- & Nano-

CHEMCATCHEM

CATALYSIS

Accepted Article

Title: Localized NiS2 Quantum Dots on g-C3N4 Nanosheets for Efficient Photocatalytic Hydrogen Production from Water

Authors: Fei Xue, Maochang Liu, Cheng Cheng, Junkai Deng, and Jinwen Shi

To be cited as: *ChemCatChem* 10.1002/cctc.201801510

Link to VoR: http://dx.doi.org/10.1002/cctc.201801510

A Journal of ChemPubSoc Europe

WILEY-VCH

www.chemcatchem.org

FULL PAPER

Localized NiS_2 Quantum Dots on g-C_3N_4 Nanosheets for Efficient Photocatalytic Hydrogen Production from Water

Fei Xue,[a] Maochang Liu,*[a][b] Cheng Cheng,[a] Junkai Deng,[c] and Jinwen Shi[a]

Abstract: Developing high-efficiency yet low-cost photocatalyst for solar hydrogen production by avoiding the use of noble metals has received adequate interest but remains a great challenge to date. This work reports a seed-mediated hydrothermal approach for the synthesis of NiS_2 quantum dots (QDs) anchored two-dimensional graphitic carbon nitride (g-C_3N_4) nanosheets. This hybrid shows superior performance toward photocatalytic H_2 evolution from water. The highest H_2 evolution rate reaches 4.841 μmol h^{-1}, with an apparent quantum efficiency of 2% at 425 nm, which is even much higher than that of Pt-modified g-C_3N_4 photocatalyst (2.865 μmol h^{-1}). Moreover, the composite presents good stability without notable activity decay after several cycled tests. It is found that NiS_2 QDs are essential for this improvement. These small nanoclusters not only benefit rapid and vectorial diffusion of photogenerated electrons from g-C_3N_4 to NiS_2, but also promote H_2 evolution by decreasing the thermodynamic overpotential for proton reduction. This work thus marks an important step toward designing good-performance and low-cost photocatalytic materials for solar H_2 conversion.

Introduction

Semiconductor-based photocatalytic H_2 evolution from water splitting has been deemed to be one of the most promising technologies to mitigate the energy and environmental crises.[1-4] Up to now, the reasonable design of sustainable and efficient visible-light-response photocatalysts is still a challenging mission. As an economical polymer semiconductor, graphitic carbon nitride (g-C_3N_4) has been identified as one of the most arresting photocatalytic materials on account of its nontoxicity, splendid endurance, appropriate band structure, convenient availability, and so forth.[5-9] However, high recombination rate of photoinduced charges as well as the limited capacity for H_2 evolution inevitably hinders its large-scale application for solar water reduction.[10-12] The last decade has witnessed significant progress by combining g-C_3N_4 with an effective cocatalyst to overcome these shortages.[13-16] This kind of heterojunction formed between the cocatalyst and g-C_3N_4 not only facilitates the rapid separation of photogenerated charge carriers but also provides numerous reactive sites to promote H_2 generation. It is worth being reminded that the noble metals such as Pt, Au, Ag, etc., are underlying cocatalyst candidates for enhancing the photocatalytic activity of g-C_3N_4.[5,17-20] Despite their extraordinary activity, the natural scarcity and preciousness of these noble metals largely limit their practicability for this technology. As a result, it is extremely attractive to explore alternative noble-metal-free cocatalysts that are sufficiently active. To date, tremendous earth-abundant transition metal compounds have been developed as cocatalysts including Ni, NiS_x (x=1 or 2), MoS_2, WS_2, $Ni_{12}P_5$, Ni_2P, $Ni(OH)_2$, etc., for boosting the photocatalytic H_2-evolution activity of g-C_3N_4.[10,11,21-29]

Very recently, transition metal sulfides have received intensive attention as active species for photocatalytic H_2 evolution.[10,21-23,30] Nonetheless, the metal sulfides decorated g-C_3N_4 are usually obtained via a solution-deposition strategy under mechanical stirring.[10,27,28] The insufficient contact between g-C_3N_4 and the cocatalyst taken by this method will lead to a weakened interfacial interaction. As a result, the stability of the composite as well as the associated charge transfer behavior has been significantly restricted. In comparison with the mechanical deposition method, hydrothermal approach has been demonstrated to be versatile to fabricate high-quality metal sulfide nanoparticles with finely tuned size and morphology.[14,21,31] It is thus reasonable to expect integration of well-defined metal sulfides onto g-C_3N_4 surface with enhanced physicochemical property via hydrothermal synthesis.

Herein, we report a facile two-step approach, involving thermal polymerization and subsequent seed-mediated mild hydrothermal treatment, for embedding uniform NiS_2 quantum dots (QDs) onto the surface of g-C_3N_4 nanosheet. The composite shows excellent and enhanced photocatalytic performance toward H_2 generation in an aqueous solution containing triethanolamine (TEOA) under visible irradiation. This amelioration is mainly attributed to the promoted charge separation efficiency at the solid interface as well as the accelerated proton reduction rate localized on NiS_2 QDs. It is expected that this work could inspire ongoing interest by extending the use of noble-metal-free cocatalyst to other highly efficient photocatalytic systems.

Results and Discussion

As characterized by TEM, the bulk g-C_3N_4 after the thermal polymerization can be easily exfoliated into nanosheet by the ultrasonic treatment (Figure S1). While the bulk g-C_3N_4 showed a clear three-dimensional stacked structure, the nanosheet was found with uniform two-dimensional layered structure. The thicknesses of the bulk g-C_3N_4 and nanosheet were about 9.0 and

---

[a] F. Xue, Prof. M. Liu, C. Cheng, Prof. J. Shi
International Research Center for Renewable Energy & State Key Laboratory of Multiphase Flow in Power Engineering,
Xi'an Jiaotong University
Xi'an, Shaanxi 710049, P. R. China
E-mail: maochangliu@mail.xjtu.edu.cnF.
[b] Prof. M. Liu
Suzhou Academy of Xi'an Jiaotong University,
Xi'an Jiaotong University
Suzhou, Jiangsu 215123, P. R. China
[c] Prof. J. Deng
State Key Laboratory for Mechanical Behavior of Materials,
Xi'an Jiaotong University
Xi'an, Shaanxi 710049, P. R. China

Supporting information for this article is given via a link at the end of the document.

3.6 nm, respectively, as determined by the atomic force microscope (AFM) (Figure S2). The ultra-thin feature of the nanosheets makes them at short-range entanglement, leading to the formation of regular crimp wave (Figure S1b, as marked by arrows). Moreover, the approximately twofold activity toward photocatalytic hydrogen production of the g-C_3N_4 nanosheet to that of the bulk counterpart provided a direct proof to certify the superiority of the exposed surface (Figure S3). This activity together with the subsequent hydrothermal treatment enables strong interaction between g-C_3N_4 and NiS_2 via seed-mediated hetero-nucleation. Despite the amounts of Ni precursor were employed, the precise NiS_2 weight percentages in final synthesized g-C_3N_4-NiS_2 composites were further determined by ICP-MS measurement, as depicted in Figure S4. Figure 1, a-c represents the typical ordinary, bright-field, and large-magnification TEM images of the hybrid that contains 25.3 wt% NiS_2. Clearly, while the nanosheet structures were largely maintained, many monodispersed QDs with a mean size (in diameter) of 2.62 nm (see Figure S5 for statistic results) were found to be anchored onto the surface of g-C_3N_4 nanosheets. As per the synthetic procedure, it is reasonable to speculate these QDs are NiS_2. To determine the nanostructure at atomic level, the composite was then investigated by high resolution TEM (HRTEM, see Figure 1d). Different from g-C_3N_4 nanosheet, the QDs were found with obvious lattice fringes. The interplanar spacings of 2.00 Å and 2.30 Å could be indexed to the characteristic NiS_2 {220} and {211} diffractions, respectively. Moreover, the intimate interfacial contact between the QDs and g-C_3N_4 surface was also clearly demonstrated. These NiS_2 QDs are expected to get the utmost out of the photogenerated electrons from g-C_3N_4, thus fundamentally facilitating the H_2-evolution kinetics. Note that when the content of NiS_2 exceeds a critical value, monolithic bulk structure instead of QDs will emerge (Figure S6). This structural transformation stems from limited capacity of entangled g-C_3N_4 to prevent the fusion and further crystallization of NiS_2 particles in the case of plentiful NiS_2 monomer. The hybrid was further investigated by the high angle annular dark field-scanning TEM (HAADF-STEM) and corresponding EDX elemental mapping analyses as shown in Figure 1, e-i. The uniform distribution densities of C and N certified the nanosheet structure of g-C_3N_4. For S and Ni, notable deviation in elemental scope was observed. While the same distribution of S and Ni explicitly illustrates the formation of NiS_2, it also indicates quantum sized NiS_2 nanoclusters localized on the surface of g-C_3N_4 nanosheets. In addition to those well-resolved larger nanoparticles, many sub-nanometer, or even atomic sized NiS_2 structures were also noticed. In fact, these sub-structures are hardly to be resolved by traditional TEM method, but could still be characterized by STEM. These results provide direct evidence for the successful fabrication of the binary g-C_3N_4/NiS_2 composite.

We further examined the crystal structure of the as-prepared g-C_3N_4/NiS_2 hybrids by powder XRD. As depicted in Figure 2, despite the poor crystallinity of g-C_3N_4, two distinct peaks centered at 13.2° and 27.5° were observed, which could be indexed to the (100) and (002) diffraction. Structurally, the two diffraction peaks stem from the in-plane ordering of tri-s-triazine motifs and periodic interlayer stacking of aromatic segments, respectively. Our result is consistent with the previously reported g-C_3N_4 synthesized via similar approach.[10-12,18,19,25,26] Generally, the position of the diffraction peak of g-C_3N_4 kept unchanged after incorporation with NiS_2, indicating the prominent property of the nanosheet to maintain the graphitic-packing layer structure. Further examination reveals that the diffraction intensity of g-C_3N_4 gradually decreases with the increment of NiS_2 content. In principle, it should be the marked inhibition effect of NiS_2 QDs on the two-dimensional structure that induces this diffraction reduction.[24] Moreover, hydrothermal treatment in the presence of $NH_3\cdot H_2O$ could induce more defect on the surface g-C_3N_4, which also contributes to the reduction of the peak intensity. In contrast, the diffraction peaks, pertaining to the characteristic diffraction pattern of standard cubic NiS_2 (JCPDS 01-089-3059),[21,32] become more evident when the content of NiS_2 increased to be more than 12.2 wt%. No NiS_2 diffraction peaks could be discerned below this content. These characteristic diffraction peaks of both g-C_3N_4 and NiS_2 in XRD profile demonstrate the successful fabrication of g-C_3N_4/NiS_2 composites.

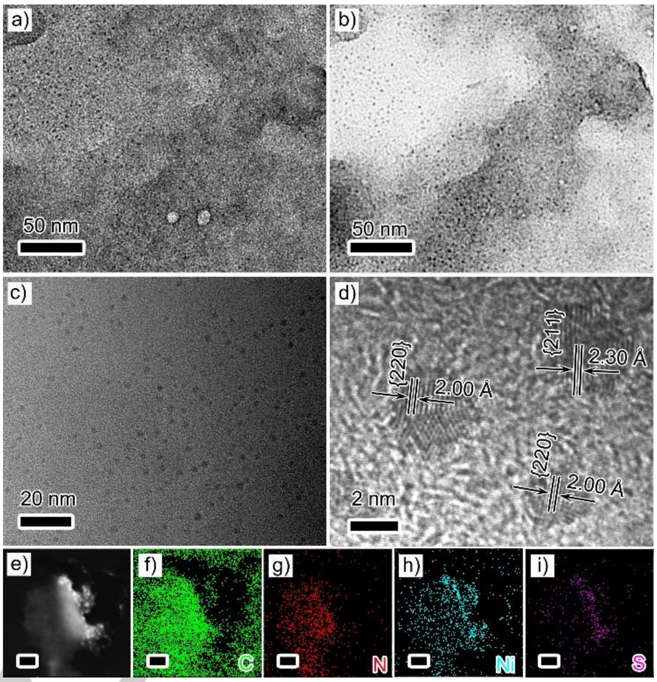

Figure 1. (a) Typical low-magnification, (b) bright-field, and (c) high-magnification TEM images of g-C_3N_4/25.3%-NiS_2 nanodots composite photocatalyst; (d) HRTEM images of g-C_3N_4/25.3%-NiS_2 nanodots composite photocatalyst; (e)-(i) STEM-EDX elemental mappings of g-C_3N_4/25.3%-NiS_2 nanodots composite photocatalyst. The scale bars in (e)-(i) are 20 nm.

To acquire insight into the chemical state and composition of g-C_3N_4/NiS_2 samples, XPS analysis was then employed (see Figure S7 for the survey spectra). Figure 3 shows the high-resolution XPS spectra of C 1s, N 1s, Ni 2p, and S 2p of g-C_3N_4/NiS_2 composite sample. For simplicity, we took the hybrid containing 25.3 wt% NiS_2 as an example and pristine g-C_3N_4 as a comparison. The identical profiles of C 1s and N 1s spectra in g-C_3N_4/NiS_2 composite and pristine g-C_3N_4 again provide a direct proof of the slight impact taken by hydrothermal treatment (see

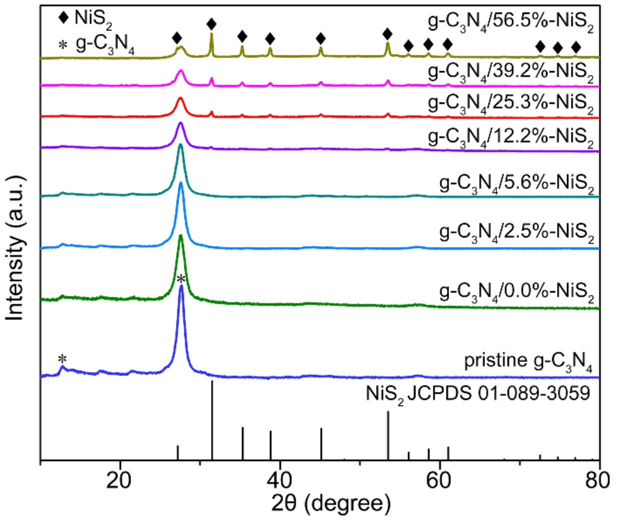

Figure 2. XRD patterns of g-C_3N_4/NiS_2 nanodots composites with different NiS_2 amounts.

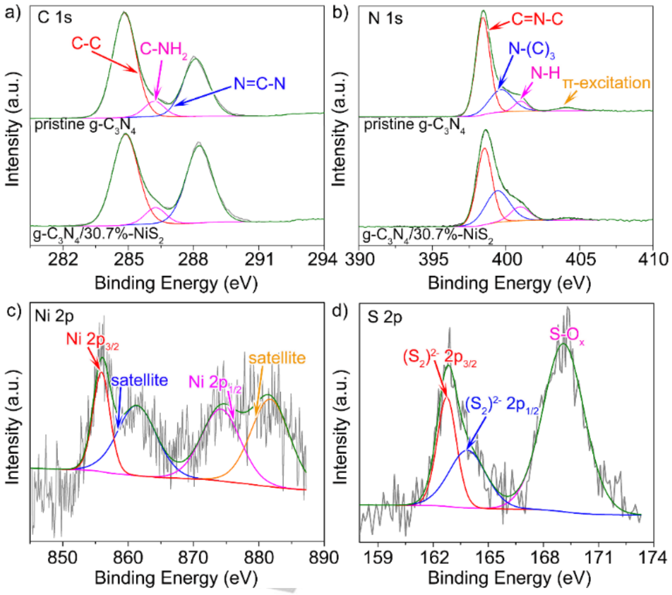

Figure 3. High-resolution XPS core-level spectra of (a) C 1s, (b) N 1s, (c) Ni 2p, and (d) S 2p for pristine g-C_3N_4 and g-C3N4/25.3%-NiS_2 composite photocatalyst, respectively.

Figure 3, a and b). Three peaks centered at 284.8, 286.2, and 288.3 eV are obtained for the C 1s spectrum after deconvolution. They are typical adventitious C species from the graphitic carbon, sp^2 hybridized C connected to -NH_2, and sp^2 C bonded to N in aromatic ring (N-C=N), respectively.[10,11,19,25] High-resolution N 1s scan can be fit into one dominant peak and three tiny ones with the binding energies of 398.5, 399.7, 401.2, and 404.2 eV, respectively. These signals derive from the sp^2 N atoms in triazine units, bridging N in N-$(C)_3$, N in the heterocycles and cyano groups (C-N-H), and π-excitation in the polymeric g-C_3N_4 structures, respectively.[10,11,19,25] For Ni 2p spectrum (Figure 3c), two typical peaks at 855.9 eV (Ni $2p_{3/2}$) and 874.1 eV (Ni $2p_{1/2}$) accompanied with two obvious satellite peaks are presented, certified the Ni(II) state.[32-34] This chemical state was further validated by the high-resolution S 2p scan, in which two typical $(S_2)^{2-}$ peaks located at 162.7 and 163.9 eV were observed (see Figure 3d).[32-34] Moreover, another conspicuous peak observed at the range of 166-172 eV can be assigned to the oxidized metal sulfide species,[33,34] which is in accordance with the Ni 2p satellite signal shown in Figure 3c.

In addition to XPS, g-C_3N_4, NiS_2, and g-C_3N_4/NiS_2 composites were also investigated by FTIR. As shown in Figure 4, the adsorption band of NiS_2 has been largely covered by that of g-C_3N_4. In this case, we did not observe any adsorption bands that represented to NiS_2 in the hybrid even 56.5 wt% NiS_2 was introduced. It also leads to the same FTIR spectra of pure g-C_3N_4 and typical g-C_3N_4/NiS_2. Taken C_3N_4/NiS_2 shown in Figure 4a as an example, the broad bands at around 3100-3400 cm^{-1} can be assigned to the stretching vibrational modes of the N-H, which are generated by the uncondensed terminal amino and -OH groups.[10,11,19,24-26] The peaks ranging from 1200 to 1700 cm^{-1} are typically a set of stretching vibration modes of aromatic heptazine-derived repeating units, including the typical sp^2 C=N stretching modes and out-of-plane bending of the sp^3 C-N bonds.[10,19,24,26] Moreover, the characteristic absorption peak centered at a smaller wavenumber, i.e., 810 cm^{-1}, should be the breathing vibration at of tri-s-triazine units,[19,26,35] indicating a more ordered in-plane structural packing motif of g-C_3N_4. Significantly, the FTIR scan without showing notable signals that represent S-N or S-C groups, suggests that no sulfide is doped into the structure of g-C_3N_4. Our FTIR results, on one hand, verify the well-maintained g-C_3N_4 nanosheet structure; on the other hand, demonstrate the intrinsic QD behavior of NiS_2.

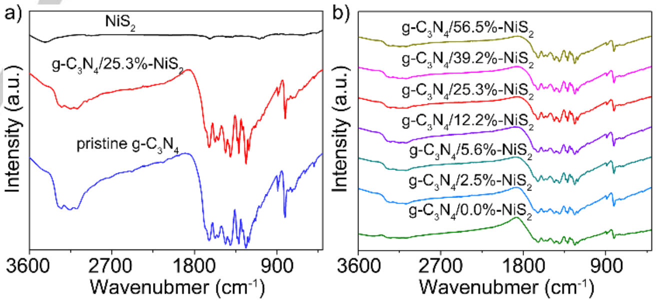

Figure 4. (a) FTIR spectra of NiS_2, pristine g-C_3N_4, and g-C_3N_4/25.3%-NiS_2 composite. (b) FTIR spectra of g-C_3N_4/NiS_2 nanodots composites with different NiS_2 contents.

The textural properties such as surface area and porous structure of pristine g-C_3N_4 and g-C_3N_4/25.3%-NiS_2 composites were also characterized by nitrogen adsorption-desorption isotherms. As clearly depicted in Figure 5, both isotherms, having typical type-IV profiles with the distinctive H3 hysteresis loops,[36] imply the predominant mesoporous character of the two photocatalysts. Significantly, the lower N_2 uptake for g-C_3N_4/25.3%-NiS_2 compared with that of pristine g-C_3N_4 indicates weakened textural behavior after the hydrothermal treatment which yet yields the narrowed pore size distribution (mean/peak pore diameter: 14.94/2.78 and 4.26/3.36 nm for pristine g-C_3N_4 and g-C_3N_4/25.3%-NiS_2, respectively, see the inset of Figure 5). The corresponding textural parameters of these two photocatalysts are summarized in Table S1. BET specific surface areas of pristine g-C_3N_4 and g-C_3N_4/25.3%-NiS_2 were calculated as 157.46 and 62.01 m^2 g^{-1}, giving corresponding pore volumes of 0.61 cm^3 g^{-1} and 0.10 cm^3 g^{-1}, respectively. It indicates the formation of partial NiS_2 quantum dots in the mesopores of g-C_3N_4, resulting in partially filled mesoporous structures.[10,37] Although the reduction in surface area and pore volume are generally unfavorable for photocatalysis, we still expect improved photocatalytic activity over the heterojunction.

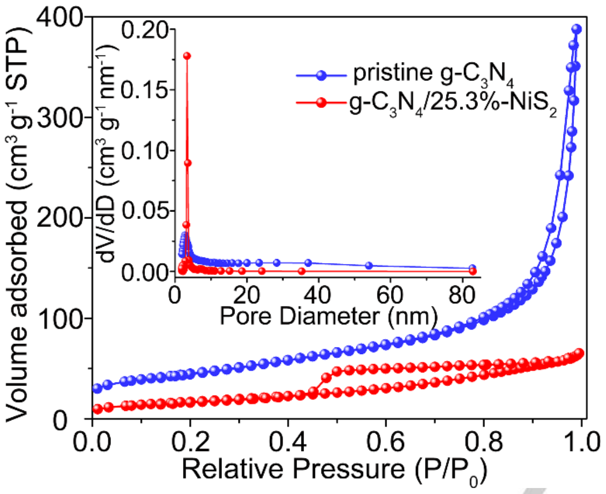

Figure 5. N_2 adsorption-desorption isotherms and the corresponding pore size distribution curves (inset) of pristine g-C_3N_4 and g-C_3N_4/25.3%-NiS_2 photocatalysts.

The as-prepared nanostructures were then evaluated as photocatalyst for visible-light-driven H_2 production from water. Blank experiments showed that no H_2 evolution was detected without either illumination or photocatalyst, indicating the photocatalytic nature of the reaction. As shown in Figure 6a, the photocatalytic activity of g-C_3N_4/NiS_2 composites was significantly improved compared to that of pure g-C_3N_4. The result indicates the surface area and pore volume are not decisive factors of the photocatalytic property. Moreover, a volcano-type trend for the mass activity as a function of loading amount of NiS_2 was obtained (Figure 6a). The highest H_2 production rate of 4.841 μmol h^{-1} was gained when the proportion of NiS_2 reached 25.3 wt%. The rapid reduction of H_2-generation activity beyond this optimized loading amount can be explained by a shielding effect of NiS_2 species. The overcrowding of NiS_2 led to a reduction of both visible-light absorption and the number of surface-active sites.[10-12,38] Note that simply hydrothermal treatment of the g-C_3N_4 without NiS_2 also could enhance the photocatalytic activity (see Figure 6a, column A and H for comparison). It indicates that both hydrothermal treatment and integration of NiS_2 could contribute to the enhancement of the photocatalytic activity for g-C_3N_4/NiS_2 composite. We also benchmarked the mass activities against the extensively investigated g-C_3N_4/Pt photocatalysts.[5,21,25,39] In this comparison, Pt was photo-deposited onto the surface of g-C_3N_4. As shown in Figure 6a, the improved photocatalytic activity by using NiS_2 is comparable or even higher than that by using Pt, indicating NiS_2 as a potential alternative for the replacing scarce Pt. More importantly, we also systematically compared the performance with that of many reported nickel-based cocatalysts modified g-C_3N_4 (Table S2). The superiority of NiS_2 clusters is thus clearly demonstrated. Meanwhile, the much lower activity of mechanical mixture g-C_3N_4 and 25.3 wt% NiS_2 than that of g-C_3N_4/25.3%-NiS_2 clearly demonstrated the advantage of close contact induced by hydrothermal treatment (see Figure 6a, column D and I). Such heterostructure was expected to be a promising and effective noble-metal-free candidate photocatalyst for H_2 evolution. We also evaluated the photostability of the composite photocatalysts by taking g-C_3N_4/30.7%-NiS_2 as an example. As shown in Figure 6b, continuous H_2 evolution without notable deactivation was achieved during a consecutive 15-h photocatalytic reaction. Figure S8a showed the typical H_2-evolution kinetics of different samples under visible-light irradiation. All samples present approximate linear H_2-evolution profiles, except the mechanical mixing g-C_3N_4/25.3%-NiS_2, in the initial 5-h reaction, confirming their relatively good photostability. The generally decreased photocatalytic activity of the mechanical mixed sample indicated the necessity of tight contact of NiS_2 nanodot and g-C_3N_4 for maintaining the stability. Figure S8b depicts the wavelength-dependent AQY of g-C_3N_4/25.3%-NiS_2 composite with respect to the corresponding UV-vis spectra. It shows a typical bandgap-transition-dependent proton reduction thus H_2-evolution behavior.[14] The AQY of g-C_3N_4/25.3%-NiS_2 composite is about 2% at 425 nm.

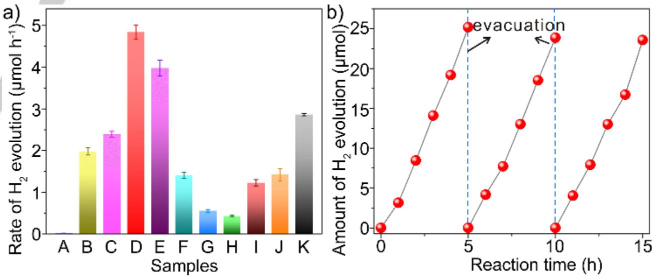

Figure 6. (a) The initial rate of hydrogen evolution rate over (A) pristine g-C_3N_4, (B) g-C_3N_4/56.5%-NiS_2, (C) g-C_3N_4/39.2%-NiS_2, (D) g-C_3N_4/25.3%-NiS_2, (E) g-C_3N_4/12.2%-NiS_2, (F) g-C_3N_4/5.6%-NiS_2, (G) g-C_3N_4/2.5%-NiS_2, (H) g-C_3N_4/0.0%-NiS_2, (I) mechanical mixture of g-C_3N_4 and 25.3 wt%-NiS_2, (J) g-C_3N_4/1%-Pt, and (K) g-C_3N_4/3%-Pt photocatalysts. (b) Time courses of recycling tests toward photocatalytic H_2 evolution over g-C_3N_4/25.3%-NiS_2 composite photocatalyst. Error bars in (a) are standard error values of three tests (n=3).

To reveal the photocatalytic mechanism that is responsible for this enhancement, the dynamics of photoinduced charge transfer was investigated by a collective use of PL, transient photocurrent measurement, EIS, and polarization curve. PL measurement is a common method to assess separation efficiency of photogenerated carriers.[10,11,40] Figure 7a shows the room-temperature PL spectra of g-C_3N_4 and g-C_3N_4/25.3%-NiS_2

photocatalysts that were excited at 370 nm. Pure g-C_3N_4 exhibited a strong intrinsic emission peak centered at ~420 nm, indicating the severe recombination of the photogenerated charge carriers in the g-C_3N_4. Although similar trend of the spectrum was observed over g-C_3N_4/25.3%-NiS_2, it showed slight blue shift and significantly decreased PL intensity. In principle, the fate of photogenerated charges determines the quenching efficiency of photoluminescence. Here, NiS_2 cocatalysts could act as charge carrier trapping center to extract electrons from g-C_3N_4 to the interface of NiS_2. As a result, the recombination of the photogenerated electrons-holes pairs can be enormously restrained, which is favorable for photocatalytic reaction. To further understand the interfacial charge separation efficiency, transient photocurrent measurement was accordingly performed. Figure 7b shows the corresponding results that were obtained under intermittent visible light illumination and at a positive bias voltage of 0.6 V. While both sample exhibit rapid and completely reversible photocurrent responses, g-C_3N_4/25.3%-NiS_2 produces an elevated photocurrent density, further demonstrating the efficaciously promoted mobility and lifetime of the charge carriers. Of particular note is that the decline of transient photocurrent derives from the detachment of film from electrode (properly because of the deficient preparation method).

EIS is a powerful electrochemical technique commonly adopted to illustrate the electron-transfer efficiency in the three-electrode systems.[10,11,41] The Nyquist impedance plots for pure g-C_3N_4 and g-C_3N_4/25.3%-NiS_2 samples are thus monitored as shown in Figure 7c. An electrical equivalent-circuit model was applied to simulate the plots (inset of Figure 7c), where R_s, CPE, and R_{ct} represent the Ohmic resistance of the electrolyte solution, constant-phase element for the electrode-electrolyte interface, and the charge-transfer resistance of contacting interface, respectively.[41] Our result indicates the semicircular Nyquist plot for both g-C_3N_4 and g-C_3N_4/25.3%-NiS_2. Nonetheless, g-C_3N_4/25.3%-NiS_2 features prominently smaller arc radius. This notion manifests a lower charge-transfer impedance and thus more smooth charge immigration toward the intimated interface between g-C_3N_4 and NiS_2. The larger semicircle radius for pristine g-C_3N_4 is imputed to the inferior electrical conductivity that hinders the electron migration from g-C_3N_4 to the back-contact electrode.[42] It also indicates that NiS_2 quantum dots in the hybrid could bridge g-C_3N_4 and back-contact electrode, thus significantly accelerating the charge separation and transport. We also measured the polarization curve for H_2 evolution over g-C_3N_4/25.3%-NiS_2 photocatalyst, together with g-C_3N_4 and pure NiS_2 photocatalysts for comparison (see Figure 7d). The tests were performed in dark with 0.5 M Na_2SO_4 act as the electrolyte, and scanning potential ranging from -0.6 to -1.8 V. The lower overpotential of NiS_2 forebodes the feasibility of being an alternative cocatalyst for photocatalytic H_2 evolution. On the contrary, pristine g-C_3N_4 produced a rather low cathodic current even the potential was set to be -1.6 V, implying the enormous energy barrier for water reduction. Significantly, an abrupt onset for cathodic current at -1.3 V can be achieved after the integration of NiS_2 and g-C_3N_4. The more pronounced cathodic current density and lower overpotential for g-C_3N_4/25.3%-NiS_2 demonstrate that the intensive electron migration could positively influence the reaction kinetics of water reduction.[43]

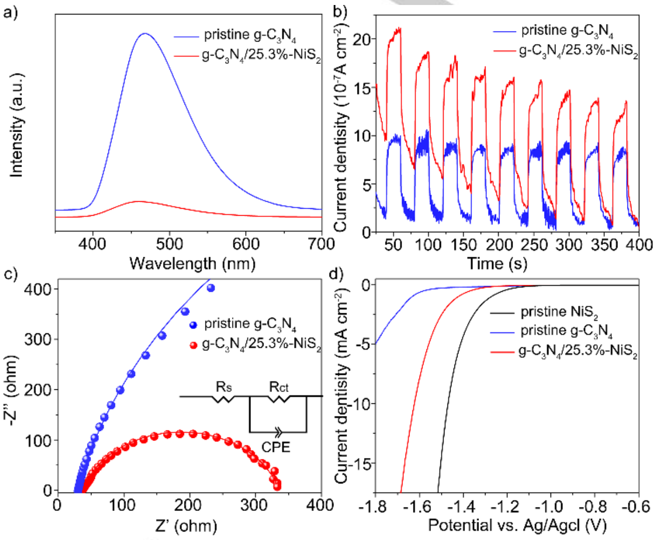

Figure 7. (a) Photoluminescence spectra of g-C_3N_4 and g-C_3N_4/25.3%-NiS_2 samples at room temperature with an excitation wavelength of 370 nm. (b) Transient photocurrent responses (I-t curves) of g-C_3N_4 and g-C_3N_4/25.3%-NiS_2 samples under visible light irradiation (> 420 nm) at a potential of 0.6 V (vs. Ag/AgCl), and (c) the corresponding Nyquist plots of electrochemical impedance spectroscopy in the dark obtained at a frequency range from 1 Hz to 10 kHz. (d) Polarization curves in the dark of pristine g-C_3N_4, pristine NiS_2, and g-C_3N_4/25.3%-NiS_2 composite. Note an aqueous solution containing 0.5 M Na_2SO_4 was employed as the electrolyte.

In addition, the optical properties of all the samples were measured using UV-vis absorption spectroscopy. As depicted in Figure S9, compared with pure g-C_3N_4, an apparent red shift of absorption band is observed for all the hydrothermal treated samples. The similar band edges indicate that the hydrothermal treatment plays a major role in narrowing the band gap. Moreover, all binary composites exhibit prominently enhanced absorption intensities with the increase of NiS_2 content, especially in the long-wavelength region. This extended light absorption, in terms of both intensity and band edge, is thus attributed to the synergistic effect between the NiS_2 and g-C_3N_4, as well as the mild hydrothermal treatment. The bandgap energy (E_g) of can be estimated by using the Kubelka-Munk method based upon the tangent lines of Tauc plots, as shown in Figure 8a, where F(R) is the diffuse absorption coefficient and hv is the photon energy.[31,40] The obtained values of the bandgap for g-C_3N_4, g-C_3N_4/0.0%-NiS_2, and g-C_3N_4/25.3%-NiS_2 are calculated to be 2.94, 2.63 and 2.62 eV, respectively. The result is consistent with the blue-shift of fluorescence spectrum (Figure 7a). In the meantime, the results again demonstrated the dominant role of hydrothermal treatment on narrowing the band gap. We next sought to determine the conduction band (CB) edge by Mott-Schottky (MS) plots over g-C_3N_4, g-C_3N_4/0.0%-NiS_2 and g-C_3N_4/30.7%-NiS_2 photocatalysts (Figure 8b). Apparently, all three samples feature in typical n-type as demonstrated by the positive tangent slopes of straight lines.[10,27] The flat band potential values of g-C_3N_4, g-C_3N_4/0.0%-

10.1002/cctc.201801510

NiS_2 and g-C_3N_4/25.3%-NiS_2 were calculated to be -1.30,-1.41 and -1.42 V (vs. Ag/AgCl), respectively. The CB edges could be accordingly obtained by negatively shift the flat band potential by -0.2 V.[44] The similar CB positions of g-C_3N_4/0.0%-NiS_2 and g-C_3N_4/25.3%-NiS_2 also certify that the band level changes stem from the hydrothermal procedure rather than NiS_2 cluster anchoring. Taken bandgap energies into consideration, the valence band (VB) positions for pristine g-C_3N_4 and g-C_3N_4/0.0%-NiS_2 are estimated to be 1.44 and 1.02 V (vs Ag/AgCl), respectively.

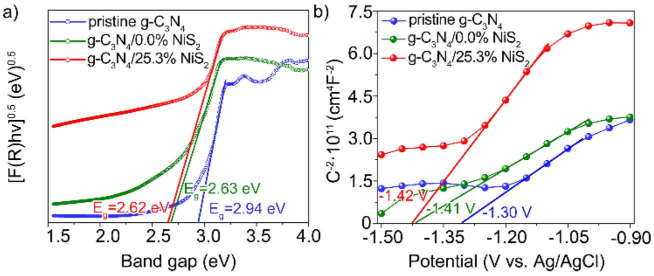

Figure 8. (a) Tauc plots of the UV-vis spectra (the relationship between $(F(R)hv)^{1/2}$ and photon energy, herein, the $(F(R)hv)^{1/2}$ donates as Kubelka-Munk function) for pristine g-C_3N_4 and g-C_3N_4/25.3%-NiS_2 photocatalyst, and (b) the corresponding Mott-Schottky (MS) plots of two different photocatalysts in the form of film electrodes. MS plots were obtained at a frequency of 1 kHz in an aqueous solution of Na_2SO_4

Consequently, the electronic band structures of these two different semiconductors can be illustrated in Scheme 1a. Specifically, the reduction potential of H^+/H_2 is positioned below the CB edge of g-C_3N_4, while the oxidation potential of H_2O to O_2 is above its VB edge. The mild hydrothermal treatment on g-C_3N_4 can elevate both the CB and VB levels, which not only enhances the reduction ability of adsorbed H^+ ions, but also promotes water oxidation. Moreover, the less negative overpotential of NiS_2 (−1.00 V vs Ag/AgCl, pH=7) allows it as a receptor to trap the photogenerated electrons from g-C_3N_4. On the basis of the above analysis, the underlying mechanism for the photocatalytic reaction on g-C_3N_4/NiS_2 is proposed as shown in Scheme 1b. Upon the irradiation of visible light, g-C_3N_4 absorbs photons via bandgap excitation to generate electrons and holes in the CB and VB, respectively. The photogenerated electrons in CB of g-C_3N_4 can easily transfer to the embedded NiS_2 quantum dots for rapid water reduction. On the other hand, the holes will diffuse within the VB of g-C_3N_4 and be captured by adsorbed TEOA molecules. More importantly, the quantum size of NiS_2 shall be also favorable for efficient electron transfer. These advantages that are induced by NiS_2 quantum dots can synergistically enhance the photocatalytic activity toward hydrogen evolution.

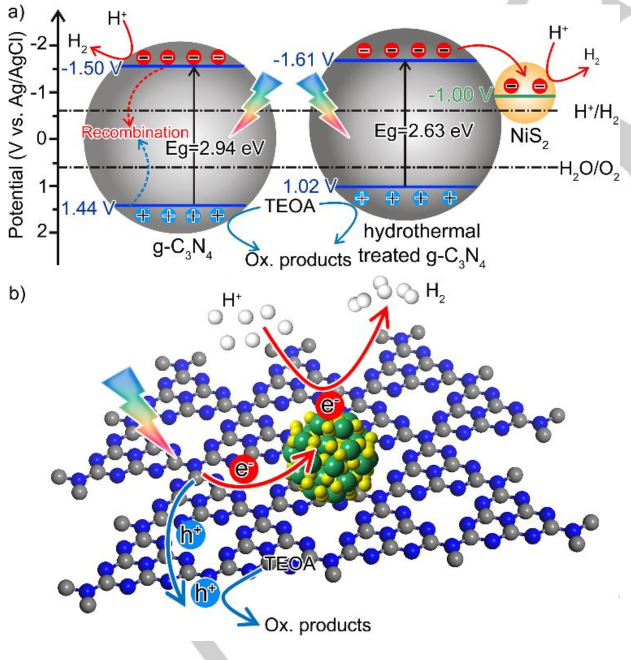

Scheme 1. (a) and (b) schematic diagrams showing the possible mechanism involved in the process of photocatalytic H_2 production over pristine g-C_3N_4 and g-C_3N_4/25.3%-NiS_2 photocatalysts under visible-light irradiation.

Conclusions

In summary, a series of g-C_3N_4/NiS_2 hybrid photocatalysts have been fabricated successfully. The success relies on a mild hydrothermal procedure for decoration of NiS_2 nanodots on the surface of g-C_3N_4. These hybrids showed notable enhancement of solar photocatalytic hydrogen production. The highest activity was achieved over g-C_3N_4/25.3%-NiS_2 photocatalyst, with a H_2 production rate of 4.841 μmol h^{-1} and an AQY of 2% at 425 nm. The efficiency is much higher than that of pristine g-C_3N_4, or even higher than that of Pt/g-C_3N_4. This improved photocatalytic property can be explained by the synergy taken by NiS_2 quantum dots for expanded visible-light harvest, improved separation and transportation efficiency of charge carriers, and reduced energy barrier for water reduction. Moreover, the composite is also relatively stable as demonstrated by cycling tests. This work provides new experimental and theoretical insights into the photocatalytic process by using an efficient but low-cost g-C_3N_4/NiS_2 hybrid photocatalyst.

Experimental Section

Chemicals and materials

Urea, triethanolamine (TEOA), thiourea, nickel (II) chloride hexahydrate ($NiCl_2·6H_2O$), sodium citrate dehydrate ($C_6H_5Na_3O_7$), ammonium hydroxide ($NH_3·H2O$), and absolute ethanol were all purchased from Sinopharm Chemical Reagent Co., Ltd. All reagents were used as received without further purification. Deionized (DI) water with a resistivity of 18.2 MΩ·cm was used for preparing all samples.

Preparation of pristine g-C_3N_4

The pristine g-C_3N_4 was synthesized with a direct polycondensation method by thermal treatment of urea under ambient pressure without the use of any additives. Typically, 10 g of urea was put into a covered alumina crucible and calcined in a muffle furnace at 600 °C for 4 h in static air at a

10.1002/cctc.201801510

ramp rate of 5 ºC min^{-1} and cooled naturally to room temperature. The product was subsequently grinded into powders thoroughly with a mortar and pestle for further processing and investigation.

Preparation of g-C_3N_4/NiS_2 composite photocatalyst

The g-C_3N_4/NiS_2 composite was synthesized using a hydrothermal method. In a typical synthesis (see Scheme S1 for detailed procedure), 40 mg of g-C_3N_4 was dispersed into 50 mL of deionized water and then the mixture was place in ultrasonic bath for 1 h to form homogeneously dispersing suspension. Then certain amounts of $NiCl_2 \cdot 6H_2O$ (2.975 mg , or 5.95 mg, or 11.9 mg, or 23.8 mg, or 35.7 mg, or 47.6 mg), $C_6H_5Na_3O_7$ (3.675 mg , or 7.35 mg, or 14.7 mg, or 29.4 mg, or 58.8 mg, or 117.6 mg), and thiourea (2.85 mg , or 5.7 mg, or 11.4 mg, or 22.8 mg, or 45.6 mg, or 91.2 mg) were added rapidly in sequence under violent stirring. After dissolution of these precursors, the pH of the suspension was adjusted to 12 by adding $NH_3 \cdot H_2O$. The obtained suspension was stirred continuously for another 10 min. After that, the mixture was transferred to a 100 mL Teflon lined autoclave and heated at 120 ºC for 24 h. After cooling to room temperature, the resultant product was separated by centrifugation and washed with deionized water and ethanol for several times to remove soluble impurities thoroughly. Finally, it was dried at 80 ºC in a vacuum oven to obtain g-C_3N_4/NiS_2 composite photocatalyst. Pure NiS_2 was prepared using the similar process except without adding g-C_3N_4.

Photocatalytic tests

Photocatalytic reactions of hydrogen production were conducted in a 50 mL side-irradiation Pyrex gas-tight circulation system with a flat optical entry window at ambient temperature using a 300 W Xe lamp equipped with a UV cut off filter (420 nm). An aluminum alloy shell was employed outside the Pyrex cell to reflect and gather the light. 5 mg of obtained photocatalyst powder was suspended under sonication in a solution containing 36 mL of water and 4 mL of triethanolamine (electron donor). The suspension was evacuated for about 20 min with N_2 gas to remove oxygen prior to the irradiation experiments. The evolved gases were analyzed by gas chromatography (Bruker GC-450) equipped with a thermal conductivity detector (TCD) and high-purity argon as the carrier gas. The apparent quantum yield (AQY) for H_2 evolution was measured using band-pass filters with various wavelengths and calculated according to the following equation:

$$AQY\ (\%) = N_e/N_p = 2N_{H2}/N_p$$

where, N_e represents for the number of reacted electrons. N_{H2} is the number of generated H_2 molecules. N_p stands for the number of incident photons.

(Photo)electrochemical Measurements

Transient photocurrent, the electrochemical impedance spectra (EIS), the polarization curve and Mott-Schottky (MS) plot analyses were carried out on a CHI600D electrochemical analyzer (Chenhua Instruments Co., Shanghai) in a standard three-electrode configuration with the sample, Ag/AgCl (in saturated KCl), and Pt plate as the working electrode, the counter electrode, and reference electrode, respectively. A sodium sulfate aqueous solution (0.5 M) served as the electrolyte in all the (photo)electrochemical measurements. For photoelectrochemical measurements, a 300 W Xe lamp equipped with a simulated solar light filter (AM 1.5) was used as the light source. The working electrodes for transient photocurrent test were fabricated using a following method. Specifically, 5 mg of catalyst was dispersed in 1.5 mL of water/ethanol (volume ratio: 1/1) solution, and then 20 μL of 10% Nafion solution (DuPont) was added to the above mixture to form a homogeneous suspension. After ultrasonic treatment for 4 h, 1 mL of dispersion solution was then spread onto a 2×3 fluorine-doped tin oxide (FTO) glass plate. Then the working electrodes were obtained after drying them under infrared lamp. For the preparation of the working electrodes for EIS, polarization curve, and MS measurements, 1 mg of sample and 10 μL of 10% Nafion (DuPont) were firstly dispersed in 1.0 mL of water/ethanol (volume ratio: 1/1) solution. The mixture was then under ultrasonic treatment for 1 h in order to get the homogeneous suspension. Subsequently, 10 μL of this dispersion was drop-casted onto the top of a glassy carbon electrode (GCE) at a diameter of 3 mm. Finally, the GCE was naturally dried under ambient temperature to get the working electrode. Time-dependent transient photocurrent responses (I-t curve) were measured at 0.4 V (vs. Ag/AgCl). For EIS measurement, a small amplitude (10 mV) alternate current (AC) signal with a frequency ranged from 1 Hz to 100 kHz at open circuit potential was provided. The same electrochemical system was also used to determine the flat-band potential of the working electrodes by the MS method. The measurements were performed in darkness by scanning the electric potential from -0.9 to -1.5 V. The impedance-potential characteristics were recorded at a frequency of 1 kHz. The polarization curves were conducted in the same system, while the bias sweep range was changed from -0.6 to -1.8 V (vs. Ag/AgCl, 10 mV/s).

Instrumentations

The powder X-ray diffraction (XRD) patterns were recorded on a PANalytical X'pert MPD Pro diffractometer using Ni-filtered Cu Kα irradiation (wavelength: 1.5406 Å) conducting at 40 kV and 40 mA. The Fourier transform infrared spectrophotometer (FTIR) spectra were collected on a Bruker Vertex 70 FTIR spectrophotometer by using the KBr pellet technique. The crystallite morphologic micrograph and microstructures were characterized by a transmission electron microscope (TEM) of FEI Tecnai G2 F30 S-Twin transmission electron microscope attached with an OXFORD MAX-80 energy-dispersive X-ray detector (EDX). X-ray photoelectron spectroscopy (XPS) was measured with a Kratos spectrometer (AXIS Ultra DLD) equipped with a standard and monochromatic Al Kα line as the excitation source (hν = 1486.6 eV). The C1s peak at 284.8 eV of adventitious carbon was used for calibration. Optical properties were determined by a Hitachi double-beam U-4100 UV-vis-near-IR spectrophotometer equipped with an integrating sphere in which $BaSO_4$ acted as the background. Nitrogen adsorption-desorption isotherms were conducted at 77 K using an Accelerated Surface Area and Porosimetry Analyzer (ASAP 2020, Micromeritics). The Brunauer-Emmett-Teller (BET) approach was employed to determine the specific surface area. Steady-state photoluminescence (PL) properties were characterized at room temperature using a time-resolved PTIQM-4 fluorescence spectrophotometer at an excitation wavelength of 370 nm. The concentrations of Ni ions were determined using a Perkin Elmer inductively coupled plasma mass spectrometer (ICP-MS, NexION 300Q). The thickness of bulk and thin layer g-C_3N_4 were measured by the atomic force microscopy (AFM, Bruker INNOVA).

Acknowledgements

This work was supported by the National Nature Science Foundation of China (No. 51502240), the Natural Science Foundation of Jiangsu Province (No. BK20150378), China Postdoctoral Science Foundation (No. 2014M560769), and the China Fundamental Research Funds for the Central Universities.

The authors also appreciate the help of Mr. Miao Wang and Mr. Kejian Lu for technical assistance.

Keywords: g-C_3N_4 • NiS_2 • photocatalysis • quantum dot • hydrogen evolution

[1] X. Chen, S. Shen, L. Guo, S. S. Mao, *Chem. Rev.* **2010**, *110*, 6503-6570.
[2] S. J. A Moniz, S. A. Shevlin, D. J. Martin, Z-X. Guo, J. Tang, *Energy Environ. Sci.* **2015**, *8*, 731-759.
[3] Y. Tachibana, L. Vayssieres, J. R. Durrant, *Nat. Photon.* **2012**, *6*, 511-518.
[4] S. Ye, R. Wang, M. Z. Wu, Y. P. Yuan, *Appl. Surf. Sci.* **2015**, *358*, 15-27.
[5] X. Wang, K. Maeda, A. Thomas, K. Takanabe, G. Xin, J. M. Carlsson, K. Domen, M. Antonietti, *Nat. Mater.* **2009**, *8*, 76-80.
[6] J. Fu, J. Yu, C. Jiang, B. Cheng, *Adv. Energy Mater*. **2017**, 1701503.
[7] W-J. Ong, L-L. Tan, Y. H. Ng, S-T. Yong, S-P. Chai, *Chem. Rev.* **2016**, *116*, 7159-7329.
[8] Y. Li, S. Ouyang, H. Xu, X. Wang, Y. Bi, Y. Zhang, J. Ye, *J. Am. Chem. Soc.* **2016**, *138*, 13289-13297.
[9] Y. Guo, J. Li, Y. Yuan, L. Li, M. Zhang, C. Zhou, Z. Lin, *Angew. Chem. Int. Ed. **2016**, 55*, 14693-14697.
[10] J. Wen, J. Xie, H. Zhang, A. Zhang, Y. Liu, X. Chen, X. Li, *ACS Appl. Mater. Interfaces* **2017**, *9*, 14031-14042.
[11] H. Zhao, S. Sun, P. Jiang, Z. J. Xu, *Chem. Eng. J.* **2017**, *315*, 296-303.
[12] C. Li, Y. Du, D. Wang, S. Yin, W. Tu, Z. Chen, M. Kraft, G. Chen, R. Xu, *Adv. Funct. Mater.* **2017**, *27*, 1604328.
[13] S. Cao, J. Low, J. Yu, M. Jaroniec, *Adv. Mater.* **2015**, *27*, 2150-2176.
[14] M. Liu, Y. Chen, J. Su, J. Shi, X. Wang, L. Guo, *Nat. Energy* **2016**, *1*, 16151.
[15] J. Ran, J. Zhang, J. Yu, M. Jaroniec, S. Z. Qiao, *Chem. Soc. Rev.* **2014**, *43*, 7787-7812.
[16] P. Ye, Xi. Liu, J. Iocozzia, Y. Yuan, L. Gu, G. Xu, Z. Lin, *J. Mater. Chem. A* **2017**, *5*, 8493-8498.
[17] Y. Di, X. Wang, A. Thomas, M. Antonietti, *ChemCatChem.* **2010**, *2*, 834-838.
[18] X. Li, W. Bi, L. Zhang, S. Tao, W. Chu, Q. Zhang, Y. Luo, C. Wu, Y. Xie, *Adv. Mater.* **2016**, *28*, 2427-2431.
[19] J. Qin, J. Huo, P. Zhang, J. Zeng, T. Wang, H. Zeng, *Nanoscale*, **2016**, *8*, 2249-2259.
[20] J. Xu, Y. Li, S. Peng, G. Lu, S. Li, *Phys. Chem. Chem. Phys*. **2013**,*15*, 7657-7665.
[21] L. Yin, Y. Yuan, S. Cao, Z. Zhang, C. Xue, *RSC Adv.* **2014**, *4*, 6127-3132.
[22] Y. Hou, A. B. Laursen, J. Zhang, G. Zhang, Y. Zhu, X. Wang, S. Dahl, I. Chorkendorff, *Angew. Chem. Int. Ed.* **2013**, *52*, 3621-3625.
[23] Y. Hou, Y. Zhu, Y. Xu, X. Wang, *Appl. Catal. B: Environ.* **2014**, *156*, 122-127.
[24] L. Kong, Y. Dong, P. Jiang, G. Wang, H. Zhang, N. L. Zhao, *J. Mater. Chem. A* **2016**, *4*, 9998-10007.
[25] J. Yu, S. Wang, B. Cheng, Z. Lin, F. N. Huang, *Catal. Sci. Technol.* **2013**, *3*, 1782-1789.
[26] D. Zeng, W-J. Ong, H. Zheng, M. Wu, Y. Chen, D-L. Peng, M-Y. Han, *J. Mater. Chem. A* **2017**, *5*, 16171-16178.
[27] Y. Lu, D. Chu, M. Zhu, Y. Du, P. Yang, *Phys. Chem. Chem. Phys.* **2015**, *17*, 17355-17361.
[28] J. Yuan, J. Wen, Y. Zhong, X. Li, Y. Fang, S. Zhang, W. Liu, *J. Mater. Chem. A* **2015**, *3*, 18244-18255.
[29] J. Xu, Y. Li, S. Peng, *Int. J. Hydrogen Energy* **2015**, *40*, 353-362.
[30] L. Jiang, L. Wang, G. Xu, L. Gu, Y. Yuan, *Sustainable Energy Fuels* **2018**, *2*, 430-435.
[31] F. Xue, W. Fu, M. Liu, X. Wang, B. Wang, L. Guo, *Int. J. Hydrogen Energy* **2016**, *41*, 20455-20464.
[32] P. Luo, H. Zhang, L. Liu, Y. Zhang, J. Deng, C. Xu, N. Hu, Y. Wang, *ACS Appl. Mater. Interfaces* **2017**, *9*, 2500-2508.
[33] P. Thangasamy, V. Maruthapandian, V. Saraswathy, M. Sathish, *Catal. Sci. Technol.* **2017**, *7*, 3591-3597.
[34] J. Yu, G. Cheng, W. Luo, *J. Mater. Chem. A* **2017**, *5*, 15838-15844.
[35] Z. Mao, J. Chen, Y. Yang, D. Wang, L. Bie, B. D. Fahlman, *ACS Appl. Mater. Interfaces* **2017**, *9*, 12427-12435.
[36] M. Thommes, K. Kaneko, A. V. Neimark, J. P. Olivier, F. Rodriguez-Reinoso, J. Rouquerol, K. S. W. Sing, *Pure Appl. Chem.* **2015**, *87*,1051-1069.
[37] X. Li, H. Li, S. Huo, Z. Li, *Kinet. Catal.* **2010**, *51*, 754-761.
[38] Z. Sun, B. Lv, J. Li, M. Xiao, X. Wang, P. Du, *J. Mater. Chem. A* **2016**, *4*, 1598-1602.
[39] G. Zhang, Z-A. Lan, L. Lin, S. Lin, X. Wang, *Chem. Sci.* **2016**, *7*, 3062-3066.
[40] X. Wang, M. Liu, Y. Chen, W. Fu, B. Wang, L. Guo, *Nanoscale* **2016**, *8*, 15970-15977.
[41] Z. Qin, Y. Chen, Z. Huang, J. Su, L. Guo, *J. Mater. Chem. A* **2017**, *5*, 19025-19035.
[42] X-X. Li, G-F. Chen, K. Xiao, N. Li, T-Y. Ma, Z-Q. Liu, *Electrochim. Acta* **2017**, *255*, 153-159.
[43] Y-P. Zhu, T-Z. Ren, Z-Y. Yuan, *ACS Appl. Mater. Interfaces* **2015**, *7*, 16850-16856.
[44] X. Li, J. Yu, J. Low, Y. Fang, J. Xiao, X. Chen, *J. Mater. Chem. A* **2015**, *3*, 2485-2534.

FULL PAPER

NiS$_2$ quantum dot successfully anchored on the surface of g-C$_3$N$_4$ promotes both vectorial charge diffusion and rapid proton reduction during photocatalytic water splitting.

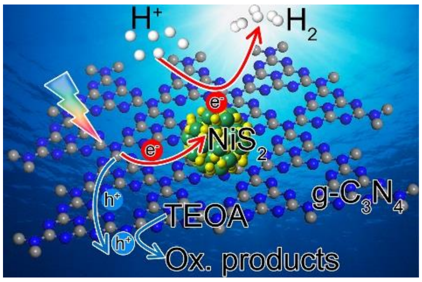

Fei Xue, Maochang Liu, Cheng Cheng*

Page No. – Page No.

Localized NiS$_2$ Quantum Dots on g-C$_3$N$_4$ Nanosheets for Efficient Photocatalytic Hydrogen Production from Water